Multi-Functional Single/Multi-Band Bandpass Filters With Co-Integrated RF Isolator, Variable Phase Shifter or Variable Attenuator Functionalities

Zixiao Zhang, *Graduate Student Member, IEEE*, and Dimitra Psychogiou, *Senior Member, IEEE*

***Abstract*— This manuscript introduces a novel RF co-design methodology that allows to co-integrate the functionality of a single-/multi-band bandpass filter (BPF), an RF switch, a variable phase shifter (VP), a variable attenuator (VA), and an RF isolator within a single multi-functional RF component. It is based on a power reconfigurable rat-race coupler (RFRC), spatiotemporally modulated (STM) resonators and a switchable phase coupling element that controls three modes of operation. These include: 1) a co-designed single/multi-band reflectionless BPF, an RF isolator (enabled/disabled by turning ON/OFF STM) and a 360°-variable phase shifter (BPF/BPFI-VP), 2) an RF switching mode and 3) a single/multi-band BPF, an RF isolator (enabled/disabled by turning ON/OFF STM) and a variable attenuator (BPF/BPFI-VA). A detailed theoretical framework is provided alongside a variety of single-band and multi-band design examples. The methodology is validated through the implementation of a single-band prototype (Prototype 1) and a dual-band prototype (Prototype 2) at 700 MHz. Specifically, Prototype 1 features a single-band BPF/BPFI-VP mode with continuously tunable phase shift of 360° while having constant transfer function (TF), a wide reflectionless bandwidth (RBW) from 375 to 1093 MHz as well as uni-directional transmission with over 20 dB directivity (D). When reconfigured in its BPF/BPFI-VA mode, a wide attenuation tuning range of 15.8 dB can be obtained with a well-preserved TF, low phase imbalance (< 5°) and D > 20 dB. Furthermore, it can be intrinsically switched-off with an isolation > 30 dB. Prototype 2 supports a third order dual-band TF with 360° tunable phase shift capability for both of its bands. Furthermore, it exhibits a RBW between 370-1200 MHz, switching-off capability with > 30 dB of IS and with D>10 dB.**

***Index Terms*— Attenuators, bandpass filter, multi-functional filter, tunable filter, phase shifters, RF co-design.**

I. Introduction

THE unprecedented growth of wireless connectivity is increasingly creating the need for RF transceivers able to support multiple standards and modes of operation while exhibiting low size, weight, and power consumption (SWaP). To facilitate their development, RF components able to functionalize a multiplicity of RF signal processing functions need to be developed to reduce the SWaP of their RF front-ends (RFFEs). Specifically, there is an increasing interest in the realization of multi-functional bandpass filters (BPFs) for their key role in suppressing interference and noise as well as due to being one of the largest components of the RFFE. As such, RF design techniques and integration concepts allowing to co-design BPFs with other essential RFFE components such as variable phase shifters (VPs) [1], [2], [3], [4], [5], [6], variable attenuators (VAs) [7], [8], [9], [10], [11], [12], [13], [14], [15], [16], [17], [18], [19], and RF isolators [20], [21], [22], [23], [24], [25], [26], [27], [28], [29], [51], [54] have been developed to facilitate the realization of phased array systems with high beam scanning resolution and low side lobe levels. These functions can only be achieved by widely tuning the phase and the amplitude of the RF signals that feed their antenna elements [30], [31], [32], [33], [34], [35].

Although a decent number of VPs [36], [37], [38], [39], [40], [41], [42] and bandpass filtering phase shifters [43], [44], [45], [46] have been reported in the open technical literature to date, co-designed bandpass filters and variable phase shifters (BPF-VPs) [1], [2], [3], [4], [5], [6] suffer from variable transfer function (TF) characteristics when large phase tuning ranges are sought. Notable examples of this drawback can be seen in the BPF-VP in [3] that is based on passive vector summation method. In this case, a second-order BPF response is obtained alongside a 320° continuous phase tuning. However, the asymmetry of the signal paths doesn't allow to preserve the TF filtering characteristics as also noted in the BPF-VPs in [1], [2], [4], and [5]. In yet another approach, the BPF-VP in [6] demonstrated relatively good TF characteristics by employing tunable external coupling networks, however its phase tuning was limited to 90°.

A wide variety of BPF-VAs have also been reported in [7], [8], [9], [10], [11], [12], [13], [14], [15], [16], [17], and [18]. They are based on on-chip implementations using transistors or graphene or utilizing the resistance change of PIN diodes under different biasing voltages. However, they are limited by a discrete number of tuning stages [7], [8], limited attenuation range (< 13 dB) [9], [10], [11], [12], [13], [14], [15], and

Manuscript received 28 March 2024; revised 24 May 2024; accepted 16 June 2024. Date of publication 23 July 2024; date of current version 29 August 2024. This work was supported by the Science Foundation Ireland (SFI) Project under Grant 20/RP/8334. This article was recommended by Associate Editor R. Gomez-Garcia. *(Corresponding author: Zixiao Zhang.)*

The authors are with the School of Engineering, University College Cork, Cork, T12 K8AF Ireland, and also with the Tyndall National Institute, Cork, T12 R5CP Ireland (e-mail: zixiao.zhang@tyndall.ie; DPsychogiou@ucc.ie).

Color versions of one or more figures in this article are available at https://doi.org/10.1109/TCSI.2024.3419583.

Digital Object Identifier 10.1109/TCSI.2024.3419583

compromised return loss or TF shapes when tuning their attenuation levels [7], [8], [9], [10], [11], [12], [13], [14], [15], [16], [17], [18]. The multi-functional RF component in [19] incorporates amplitude tunability into a BPF-VP, however it is limited to low order (2^{nd}) TFs whose characteristics change while tuning the phase of the output RF signals. Overall, none of the reported BPF-VPs or BPF-VAs facilitates scalability to higher order TFs or multi-band operability, limiting the application of these devices.

In yet another approach, BPFs are co-designed with RF isolators (BPFIs; also named non-reciprocal filters) to facilitate unidirectional transmission [20]. Notable demonstrations of this approach include the use of magnetically-biased components [21], [22], exploiting the inherent non-reciprocity of transistors [23], [24] and spatiotemporal modulation (STM), where resonators are modulated with phased-shifted low-frequency AC signals [25], [26], [27], [28], [29], [51], [54]. Among them, STM has been widely exploited for the realization of BPFIs due to its compact size, cost-effectiveness, and ease of integration. However, their transmission phase or attenuation can't be tuned. A BPFI with VP capabilities (i.e., BPFI-VP) was demonstrated in [29]. It is based on filtering rat-race coupler (RFRC) and (STM) resonators. However, it showed limited TF selectivity (up to 2^{nd} order) and fairly low directivity of about 10 dB.

Considering the limitations of the state-of-the-art (SOA), this paper presents a comprehensive design methodology for the realization of a new class of a multi-functional RF component that incorporates the simultaneous functionality of a single- or multi-band BPF, a VP with 360° continuously-tunable phase shift, a VA with theoretically infinitely-tunable attenuation, an RF switch and an RF isolator that can be materialized within the volume of a single RF component. Specifically, the proposed concept facilitates the implementation of three multi-functional modes of operation, namely: 1) a single/multi-band reflectionless BPF/BPFI-VP mode of operation, 2) an intrinsically switched-off response and 3) a single/multi-band BPF/BPFI-VA mode of operation.

The proposed multi-functional BPF/BPFI-VA/VP concept builds upon the work in [47]. However, it further expands this concept by demonstrating: 1) enhanced multi-functionality by incorporating within the same RF component the additional function of an RF isolator alongside the function of a BPF, a VP and a VA; 2) its scalability for the realization of higher-order TFs; 3) scalability to quasi-elliptic or multi-band BPF-VP/BPFI-VA modes of operation; 4) a comprehensive theoretical framework supported by a generic synthesis method of the RFRC, detailed design guidelines for high-order and multi-band TFs and a comprehensive trade-off analysis for incorporating directionality and 5) practical validation through high-order dual-band prototypes to showcase its enhanced capabilities. The aforementioned capabilities allow to reduce the RFFE footprint by integrating multiple functionalities into a single device, eliminating the need for separate modules as required in classic RFFE implementations based on in-series cascaded component implementations. Furthermore, by reusing circuit elements, such as employing the same input and output power dividers and rat-race coupler for the realization of the VP and the VA, IL and circuit complexity can be significantly reduced. In terms of practical applications, the proposed multi-functional RF component can be enabling for emerging phased antenna arrays and MIMO antenna systems, which require flexible beam-steering capabilities and high isolation between their different antenna elements or the transmit and receive modules of RF transceivers. Additionally, this methodology is well-suited for joint communication and radar systems, where integration of multiple functions into a single, compact device can lead to significant improvements in performance and efficiency.

The manuscript is organized as follows. Section II presents the theoretical foundations of the reconfigurable RFRC through coupled resonator techniques. Six different design examples are provided to showcase the RFRC's flexibility in supporting various TF profiles. This section also explores the phase and amplitude tuning schemes when reconfigured in the VP and VA mode of operation. The STM concept is also introduced, and the non-reciprocal behavior of the BPFI-VP and BPFI-VA modes of operation are analyzed through parametric studies. Section III discusses the experimental validation of the concept through the manufacturing and testing of two prototypes. Specifically, Prototype 1 demonstrates a reconfigurable third order single-band BPF/BPFI-VP response, a third-order single-band BPF/BPFI-VA response, and an intrinsically switched-off mode of operation. Prototype 2 functionalizes a third-order dual-band BPF/BPFI-VP mode of operation and an intrinsically switched-off response. Section IV summarizes the main contributions of this work.

II. Theoretical Foundations

The block diagram of the proposed multi-functional RF component concept is illustrated in Fig. 1 alongside the conceptual S-parameters of its three reconfigurable modes of operation. It consists of two power dividers, each followed by two coupling elements with static phase (φ_1) or reconfigurable phase (φ_2) and an RFRC as shown in Fig. 1(a). The multi-functional RF component functionalizes different modes of operation which can be obtained as follows:

1) When $\varphi_2 - \varphi_1 = 90°$, the BPF/BPFI-VP mode can be obtained while having a symmetric-input-reflectionless response as shown in the conceptual S-parameters in Fig. 1(b). In this case, the insertion phase can be tuned between 0°-360° by altering the RFRC's coupling strength.

2) When $\varphi_2 - \varphi_1 = 90°$, the couplings between P_1, P_4 and P_2, P_3 inside the RFRC are set to zero while the couplings between P_1, P_3 and P_2, P_4 are the same, the multi-functional component operates in the switching-off mode of operation as indicated in Fig. 1(c).

3) When $\varphi_2 - \varphi_1 = 0°$, the multi-functional component operates in the BPF/BPFI-VA mode and can achieve an attenuation range from 0 to ∞ dB, as demonstrated in Fig. 1(d).

4) For both the BPFI-VP and the BPFI-VA modes of operation, the isolator functionality can be enabled/disabled by turning ON/OFF the STM to reconfigure the signal transmission mode from uni-directional to bi-directional.

The characteristics of each of the elements of the multi-functional RF component alongside the operating

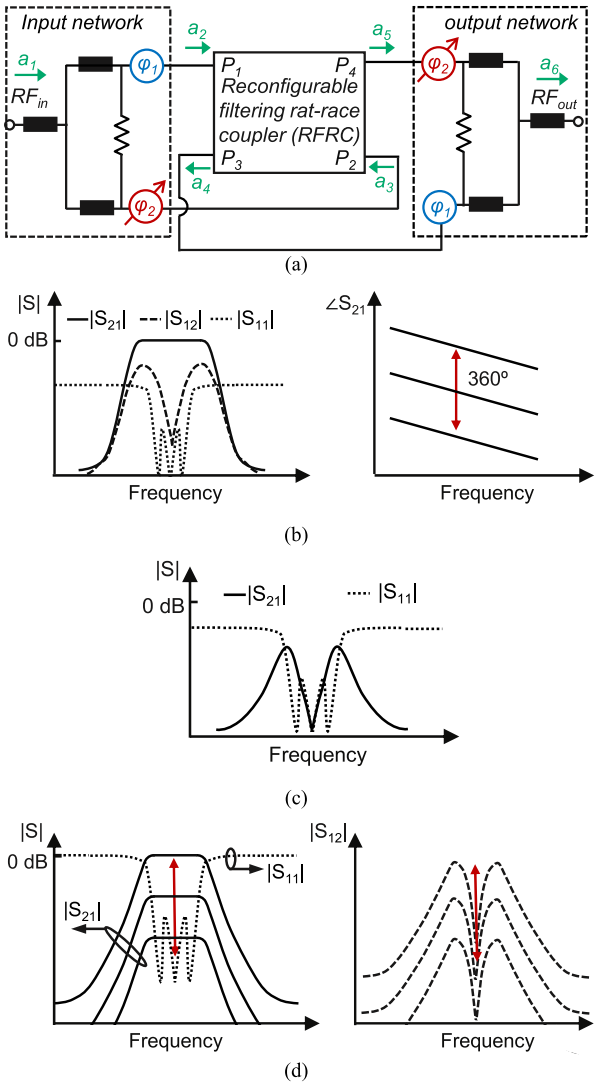

Fig. 1. (a) Block diagram of the proposed multi-functional RF component with three reconfigurable modes of operation: 1) a BPF/BPFI-VP mode, 2) an intrinsically-switched-off mode and 3) a BPF/BPFI-VA mode. Reconfigurability between the three modes is achieved through the phase variation couplings φ_1 and φ_2 as well as the couplings in RFRC. (b) Reflectionless BPF/BPFI-VP mode of operation when $\varphi_2 - \varphi_1 = 90°$ with a 0-360° of phase shift by altering the coupling ratio of the RFRC. (c) Intrinsic switching-off mode of operation when $\varphi_2 - \varphi_1 = 90°$ and the couplings between P_1, P_4 and P_2, P_3 are zero while the couplings between P_1, P_3 and P_2, P_4 are the same. (d) BPF/BPFI-VA mode of operation when $\varphi_2 - \varphi_1 = 0°$ with a continously tunable attenuation level between 0 and ∞ dB by altering the coupling ratio of the RFRC.

principles of each mode of operation are detailed in the next sections through analytical equations and a wide range of design examples.

A. Reconfigurable Filtering Rat-Race Coupler (RFRC)

Fig. 2(a) demonstrates the coupling routing diagram (CRD) of the RFRC which is the most important building block of the multi-functional RF component. It consists of four synchronously tuned resonators R_1-R_4− denoted by black circles. The resonators are coupled through reconfigurable couplings, denoted as xM_m and yM_n, with x and y indicating the coupling polarity and are limited to values of +1 or -1. M_1 indicates the external coupling which is connected to the

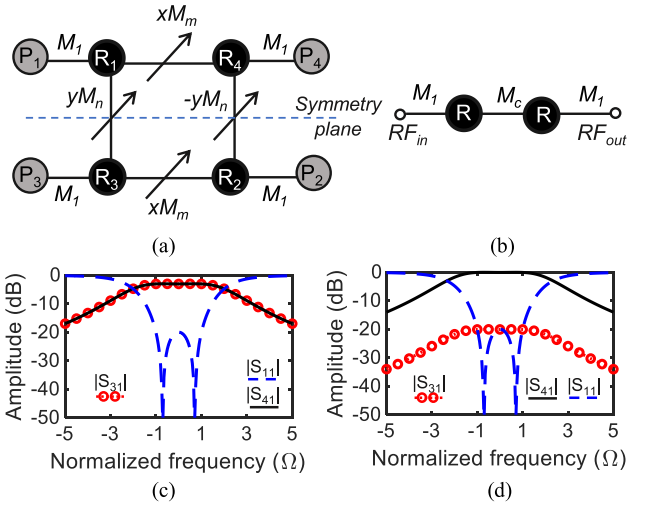

Fig. 2. (a) CRD of a RFRC functionalizing second-order TFs at its output ports P_3, P_4. (b) CRD of the equivalent filtering network for each of its RF signal propagation paths. (c) Synthesized scatering parameters of the RFRC when k =1 and M_1 =1.226, M_c =1.662, M_m = M_n =1.1752. (d) Synthesized scatering parameters of the RFRC when k =100 and M_1 =1.226, M_c =1.662, M_m =1.6538, M_n =0.1654.

phase coupling elements φ_1 and φ_2. Due to the RFRC being symmetrical, it can be analyzed using even and odd mode analysis as in [48] and [49] which leads to the S-parameters that outlined in equations (1) to (4). As shown in (2) and (3), M_m and M_n determine the output power distribution and this four-port network functions as a rat-race coupler, characterized by a power division ratio (k), which is described in (5). Specifically, the RF power from P_1 is divided based on k towards P_3 and P_4, while P_2 remains isolated.

From a filtering perspective, the RFRC facilitates the realization of a second-order filtering TF, whose characteristics can be determined by comparing the polynomial expressions in (1)-(3) with those of a second-order BPF [49]. Setting $M_m^2 + M_n^2$ to a constant value M_c^2 as defined in (6) ensures that the input reflection coefficient (S_{11}) and the denominators of S_{41} and S_{31} stay constant across variations of k, thus maintaining the TF shape while allowing to alter the power division ratio between P_3, P_4 whose response can be considered equivalent to the one obtained by the second-order CRD in Fig. 2(b).

$$S_{11} = S_{22} = S_{33} = S_{44} = \frac{s^2 + M_m^2 + M_n^2 - M_1^4}{s^2 + 2sM_1^2 + M_m^2 + M_n^2 + M_1^4} \tag{1}$$

$$S_{14} = S_{41} = S_{23} = S_{32} = \frac{2jM_1^2 M_m}{s^2 + 2sM_1^2 + M_m^2 + M_n^2 + M_1^4} \tag{2}$$

$$S_{13} = S_{31} = -S_{24} = -S_{42} = \frac{2jM_1^2 M_n}{s^2 + 2sM_1^2 + M_m^2 + M_n^2 + M_1^4} \tag{3}$$

$$S_{12} = S_{21} = S_{34} = S_{43} = 0 \tag{4}$$

$$k = \frac{M_m^2}{M_n^2} \tag{5}$$

$$M_m^2 + M_n^2 = M_c^2 \tag{6}$$

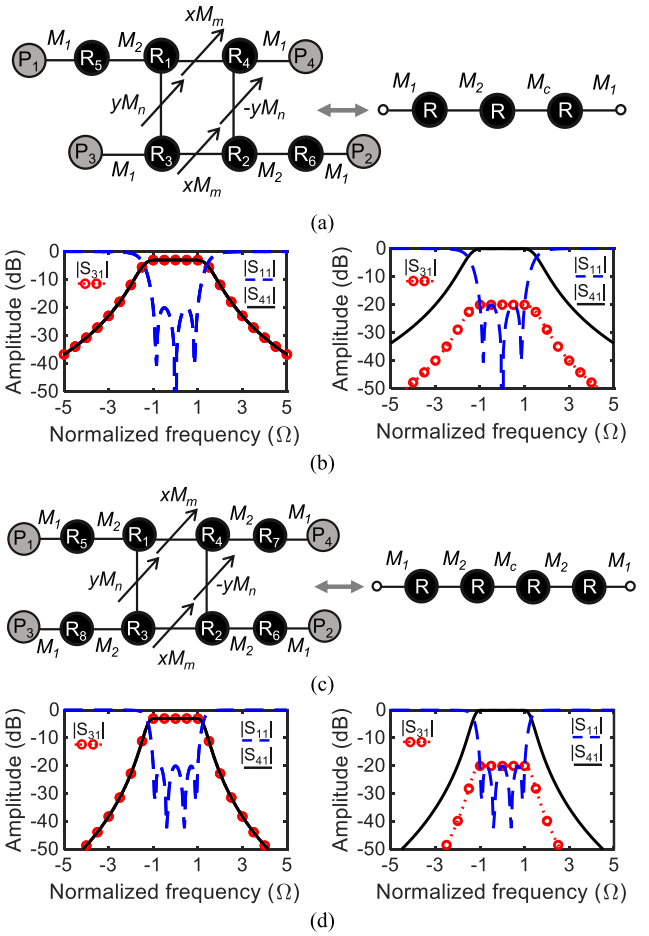

Fig. 3. Order scalability of the proposed RFRC. (a) CRD of a RFRC functionalizing third-order TFs at its output ports P_3, P_4 and its equivalent filtering CRD for each of its RF signal propagation paths. (b) Synthesized scatering parameters of the RFRC when k =1 or 100. When k = 1: M_m = M_n = 0.7295. When k =100: M_m =1.0266, M_n =0.1027. The rest of the coupling coefficients are: M_1 =1.083663, M_2 = M_c =1.0317. (c) CRD of a RFRC functionalizing fourth-order TFs at its output ports P_3, P_4 and its equivalent filtering CRD for each of its RF signal propagation paths. (d) Synthesized scatering parameters of the RFRC when k =1 or 100. When k = 1: M_m = M_n = 0.4953. When k =100: M_m =0.697, M_n =0.0697. The rest of the coupling coefficients are: M_1 =1.0362, M_2 =0.9116, M_c =0.7005.

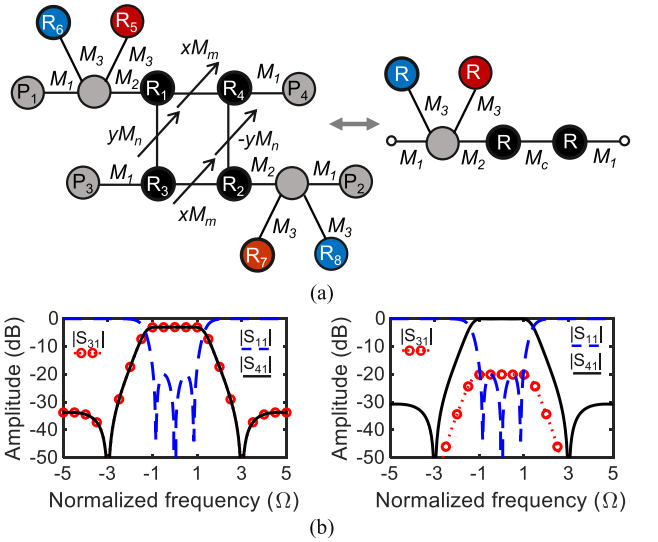

Fig. 4. CRD of the RFRC functionalizing quasi-elliptic third order TFs with two zero at its output ports P_3, P_4 and its equivalent filtering CRD for each of its RF signal propagation paths. The nodes in the same color have the same self resonting coefficients. The grey nodes are non-resonating nodes. (b) Synthesized scatering parameters of the RFRC for k =1, 100. When k = 1, M_m = M_n = 0.6998. When k =100, M_m =0.9848, M_n =0.0985. The rest of the coupling coefficients are: M_1 =1.05614, M_2 =0.98972, M_3 =2.0512, M_c =0.98972, M_{66} = M_{88} = 3, M_{55} = M_{77} =-3.

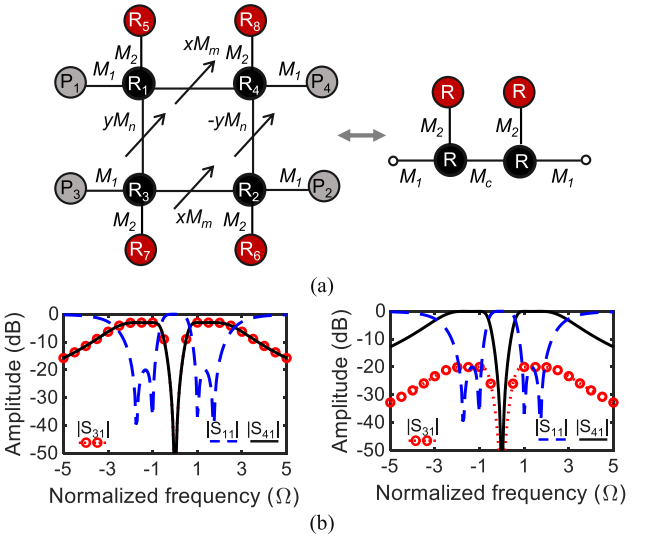

Fig. 5. (a) CRD of the RFRC functionalizing a dual-band second-order TFs at its output ports P_3, P_4 using split-type resonators and its equivalent filtering CRD for each of its RF signal propagation paths. (b) Synthesized scatering parameters of the RFRC when k =1 or 100. When k = 1: M_m = M_n = 1.1752. When k =100: M_m = 1.6538, M_n = 0.1654. The rest of the coupling coefficients are: M_1 = 1.226, M_2 = 1.326, M_c =1.662.

To demonstrate this functionality, the RFRC has been designed for a second order Chebyshev TF with a 0.043 dB ripple level (return loss of 20 dB) and its responses are shown in Figs. 2(c), (d) for different k =1 and 100, respectively. They have been obtained by calculating M_1, M_2, M_c of the CRD in Fig. 2 (b) as in any conventional second-order BPF as described in [50]. Then M_n and M_m are calculated from (5) and (6). As indicated in Fig. 2(c), the input power is equally coupled to P_3 and P_4 when k equals to 1. When k = 100, the power delivered to P_4 is 20 dB larger than that of P_3 as indicated in Fig. 2(d). Notably, second order Chebyshev responses are formed for both cases and the return loss remains the same when varying k.

The RFRC can be scaled to accommodate higher-order, quasi-elliptic as well as multi-band TFs as it is further illustrated in Figs. 3 to 6 through its corresponding CRDs in Figs 3(a), 3(c), 4(a), 5(a) and 6(a). By applying the same design methodology to these configurations and utilizing the coupling coefficients specified in the captions, various types of TFs can be realized, as demonstrated in Figs 3(b), 3(d), 4(b), 5(b) and 6(b). Specifically, the topology depicted in Fig. 3 illustrates a method for scaling the filter order, showcasing how third-order and fourth-order TFs can be obtained. Additionally, Fig. 4 presents a method for implementing a quasi-elliptic transfer function, highlighting the flexibility of the proposed structure. In these cases, all the black resonators are resonating at the same frequency and create the poles of the TF. The blue and red resonating nodes, along with the

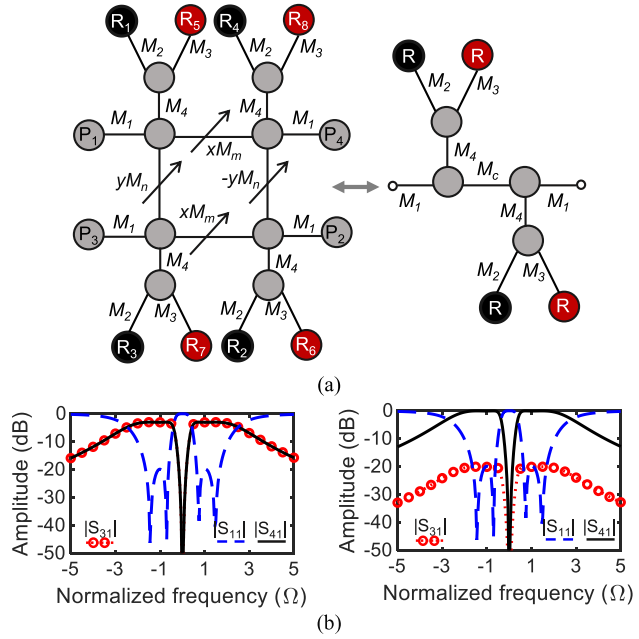

Fig. 6. (a) CRD of the RFRC functionalizing a dual-band second-order TFs at its output ports P_3, P_4 using multi-resonant resonators and its equivalent filtering CRD for each of its RF signal propagation paths. The black nodes have the same self resonting coefficients and the red ones have the same self resonting coefficients. The grey nodes are non-resonating nodes. (b) Synthesized scatering parameters of the RFRC for k =1, 100. When k = 1, $M_m = M_n = 0.5841$. When k =100, $M_m = 0.8219$, $M_n = 0.0822$. The rest of the coupling coefficients are: $M_1 = 0.8635$, $M_2 = 0.78567$, M_3 =0.7823, M_4 =0.771, Mc =0.826, $M_{11} = M_{22} = M_{33} = M_{44}$ =-1.04, $M_{55} = M_{66} = M_{77} = M_{88} = 1.0085$.

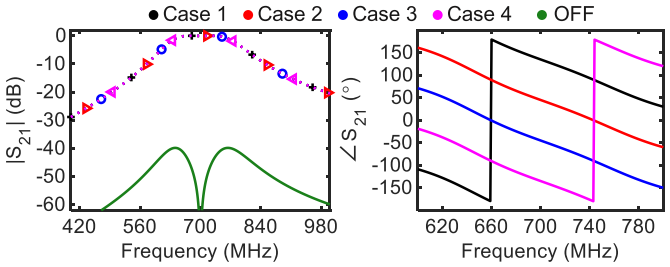

Fig. 7. Simulated S-parameters using the CRD in Fig.2 (a) at BPF-VP mode. Case 1: x =-1, y +1, Case 2: $x = y$ =+1, Case 3: x =+1, y =-1, Case 4: $x = y$ =-1 and k =1 for all the four cases.

grey non-resonating node, form a multi-resonant cell. This cell introduces two transmission zeros (TZs) and one additional pole. The TZs are located at the resonant frequencies of the blue and red nodes. The additional pole occurs at the frequency where the two paths in the multi-resonant cell exhibit equal magnitude but opposite sign admittances [51].

To showcase the versatility and practicality of the proposed synthesis approach, two distinct CRDs commonly employed for the realization of multi-band TFs are explored in Figs. 5 and 6. The CRD in Fig. 5 is based on a split-type resonator approach [52], whereas the one in Fig. 6 is using multi-resonant resonators [53]. Whereas both topologies lead to identical multi-band responses, the CRD in Fig.5 based on split-type resonators uses less elements, whereas the one based on multi-resonant resonators in Fig. 6 allows for bands that can be tuned independently. Notably, in all the synthesized

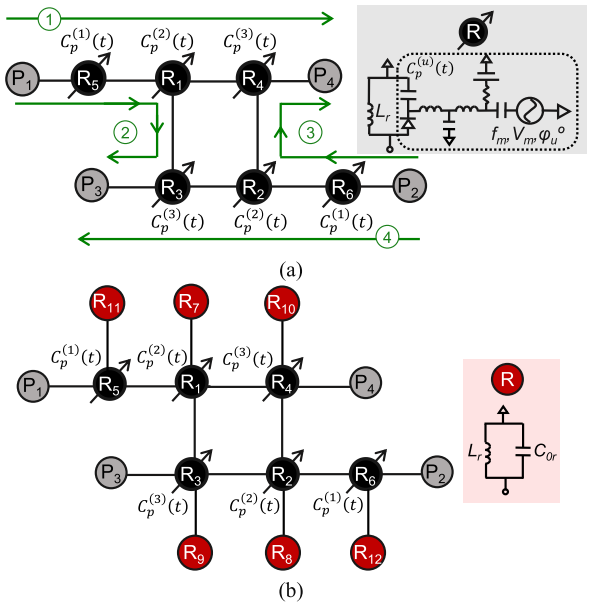

Fig. 8. STM RFRC concepts allow to incorporate the isolator functionality.(a) CRD for the realization of a third order single-band response. (b) CRD for the realization of a third order dual-band response. In these CRDs, the black circles represent STM resonators and the red circles denote static resonators. The inductance for all of the resonators is set equal to L_r = 5.17 nH. The capacitance of the static resonators and the static capacitance of the STM resonators are C_{0r} =10 pF.

instances for these five different topologies shown in Figs. 3 to 6, the desired responses are achieved with well-preserved transfer function at the output ports and $|S_{11}|$ remaining constant as k is adjusted. This characteristic facilitates the constant TF characteristics of the proposed multi-functional RF component when its phase or amplitude is being tuned as it will be discussed in the next sections.

B. Mode 1: RF Co-Designed Bandpass Filter, Isolator and Variable Phase Shifter (BPF/BPFI-VP)

The BPFI-VP mode of operation is obtained when the STM is ON and φ_2-φ_1 =90°, facilitating a filtering response in the direction of propagation with a 360° continuously adjustable phase shift and RF signal cancellation in the reverse direction as depicted in Fig. 1(b). In this mode of operation, the isolator function can be enabled/disabled by turning ON/OFF the STM. To best analyze its behavior, we first consider the case when STM is OFF, leading to a BPF-VP function whose response can be described by the relationships listed in (7) to (13). Specifically, (7) quantifies the incident power at P_1 and P_2 of the RFRC, with θ_{pd} being a fixed phase delay induced by the input network. Subsequently, (8) details the scattering matrix (S_c) of the RFRC at the center frequency, and (9) details the power relationship within the RFRC. Combining (7)-(9), the output power wave a_4 at P_3 can be expressed in relation to the input power a_1. Then using (10), the total output power wave a_6 can be correlated with a_4, and consequently with a_1, leading to (11). Using (11), the amplitude $|S_{21}|$ and the phase $\angle S_{21}$ of the BPF-VP mode of operation (STM is OFF) can be calculated using (12) and (13). Notably, $|S_{21}|$ maintains a value of 1, while the insertion phase varies as a function of

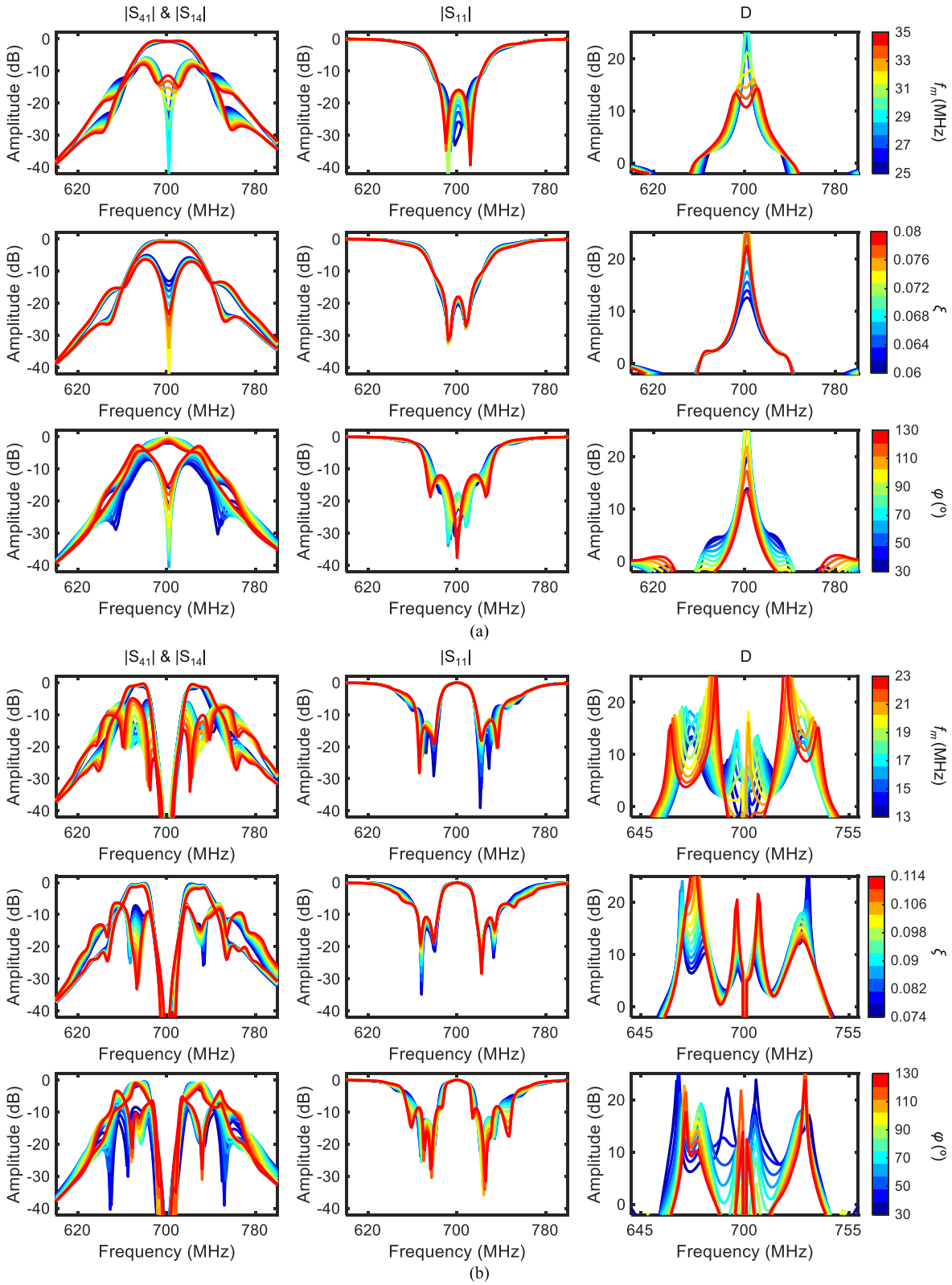

Fig. 9. S-parameters of the RFRCs in Fig. 8 when varying f_m, ξ and φ. (a) Third order single-band response using the CRD in Fig. 8(a). (b) Third order dual-band response using the CRD in Fig. 8(b).

x, y, and k, as specified in (14) to (17).

$$a_2 = \frac{a_1}{\sqrt{2}} e^{j\theta_{pd}}, a_3 = a_2 e^{-j\frac{\pi}{2}} \tag{7}$$

$$[S_c] = \frac{-j}{\sqrt{k+1}} \begin{bmatrix} 0 & 0 & y \times 1 & x\sqrt{k} \\ 0 & 0 & x\sqrt{k} & -y \times 1 \\ y \times 1 & x\sqrt{k} & 0 & 0 \\ x\sqrt{k} & -y \times 1 & 0 & 0 \end{bmatrix} \tag{8}$$

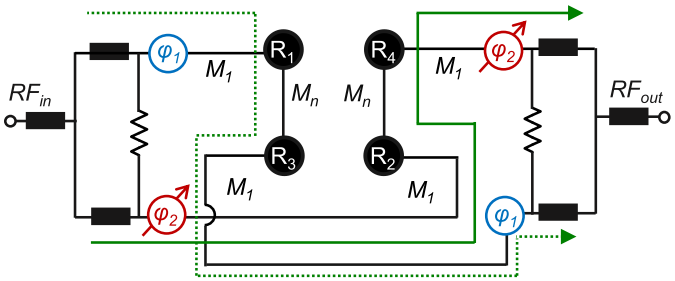

Fig. 10. RF signal flow in the multi-functional RF component when $\varphi_2 - \varphi_1 = 90°$, M_m =0 (i.e., Mode 2). In this configuration it functionalizes an intrinsically switched-off response.

$$a_4 = S_{c_3 1} a_2 + S_{c_3 2} a_3 \tag{9}$$

$$a_6 = \sqrt{2} e^{j\theta_{pd}} a_4 \tag{10}$$

$$|a_6| = |a_1|\,, \angle a_6 = \theta_{pd} + arctan(\frac{-x\sqrt{k} - jy}{\sqrt{k+1}}) + \angle a_1 \tag{11}$$

$$|S_{21}| = \frac{|a_6|}{|a_1|} = 1 \tag{12}$$

$$\angle S_{21} = \angle a_6 - \angle a_1 = 2\theta_{pd} + arctan(\frac{-x\sqrt{k} - jy}{\sqrt{k+1}}) \tag{13}$$

$$-180^{\circ} \le \angle S_{21} \le -90^{\circ}, x = 1, y = 1 \tag{14}$$

$$90^{\circ} \le \angle S_{21} \le 180^{\circ}, x = 1, y = -1 \tag{15}$$

$$90^{\circ} \le \angle S_{21} \le 180^{\circ}, x = 1, y = -1 \tag{16}$$

$$-90^{\circ} \le \angle S_{21} \le 0^{\circ}, x = -1, y = 1 \tag{17}$$

It should be noted that for each x and y combination, adjusting k from 0 to ∞ yields a 90° phase tuning, and all combinations result in an overall 360° phase tuning. Additionally, due to the 90° phase difference of the phase coupling elements φ_1 and φ_2, the RF signals reflected from the RFRC outside of the passband at P_1 and P_2 have equal amplitude and 90° phase difference. When these signals encounter the phase coupling elements again, they undergo an additional 90° phase shift, resulting in a total phase difference of 180° between them. Consequently, by the time these signals reach the output ports of the Wilkinson power divider, they have equal amplitudes but a 180° phase difference. Consequently, the two signals cancel each other out, preventing any reflection back to the input and ensuring a reflectionless response.

To showcase the continuous phase tuning capability of the multi-functional RF component, circuit simulations were carried out using the CRD in Fig. 2 and ideal phase couplings with φ_2-φ_1 =90°. The amplitude and phase responses of S_{21} for four distinct phase tuning cases are provided in Fig. 7. In this case, k is set equal to 1 while x and y are varied across the four different combinations, as specified in (14) to (17). As shown, a constant filtering TF is maintained for all variable phase tuning states.

When the STM is turned ON, the isolator function can be enabled, and the device is working at its BPFI-VP mode. The STM is enabled by modulating the resonators of the RFRC in time and in space (i.e, STM) with progressively phase-shifted low-frequency AC signals. To further demonstrate the operating principles of STM, two RFRC design examples are

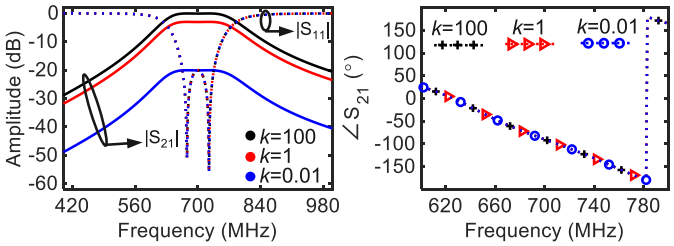

Fig. 11. Simulated S-parameters using the CRD in Fig.2 at BPF-VA mode for different values of k.

considered in Fig. 8. Specifically, Fig. 8(a) depicts the CRD of a STM RFRC that exhibits a single-band third order TF, while Fig. 8(b) showcases a topology that facilitates a third order dual-band TF. The coupling coefficients are determined using the design methodology in Section II-A and the STM details of the applied AC signals are noted on the CRDs in Fig. 8.

As presented in Fig. 8(a), the STM resonators can be implemented by a parallel connection of LC network with a static inductance L_r and a time-varying capacitances $C_p^{(u)}(t)$. The capacitances of the resonators should satisfy (18), where C_{0r} denotes the static capacitance, f_m is the AC signal frequency, ξ is the modulation index controlled by the amplitude of the AC signals and φ_u is the modulation phase. In contrast to the conventional BPFIs in [25], these AC signals need to be carefully introduced to adjacent resonators and along each propagation path, so that they maintain a consistent phase

$$C_p^{(u)}(t) = C_{0r}[1 + \xi cos(2\pi f_m t + \varphi_u)] \tag{18}$$

difference φ. For instance, in Fig. 8(a), when power is introduced at P_1 and P_2, it is subsequently directed to P_3 and P_4, forming four distinct signal paths within the topology as marked and labeled in green. This arrangement results in a sequential phase shift across all four paths. In the RFRC in Fig. 8(b), only the resonators depicted in black need to be modulated, as they form the passband of the filter. Conversely, the resonators marked in red create the notch between the two bands, and thus do not need to be modulated. By carefully selecting the aforementioned modulation parameters, unilateral transmission can be achieved, as it is conceptually illustrated in Figs. 1(b) and 1(d) by the broken dashed lines.

The STM parameters f_m, ξ and φ result in alternative performance trade-offs for the BPFI in terms of insertion loss (IL), directivity (D), and return loss (RL) as illustrated in Fig. 9. They have been obtained using schematic circuit simulations in ADS Keysight using ideal lumped LC components and non-linear capacitors for the realization of STM resonators. Their element values are provided in the caption of Fig.8. In these cases, the power ratio of the RFRCs is set to 100 and the polarity of the reconfigurable couplings is chosen as $x = 1$, $y = 1$. The obtained performances are provided in Fig. 9, where the amplitudes of the S-parameters ($|S_{11}|$, $|S_{14}|$, $|S_{41}|$) and the directivity ($D = |S_{41}| - |S_{14}|$) are plotted against frequency for different modulation parameters. As it is shown in Fig. 9(a), as f_m decreases, D increases, whereas IL decreases. Furthermore, when looking at the first

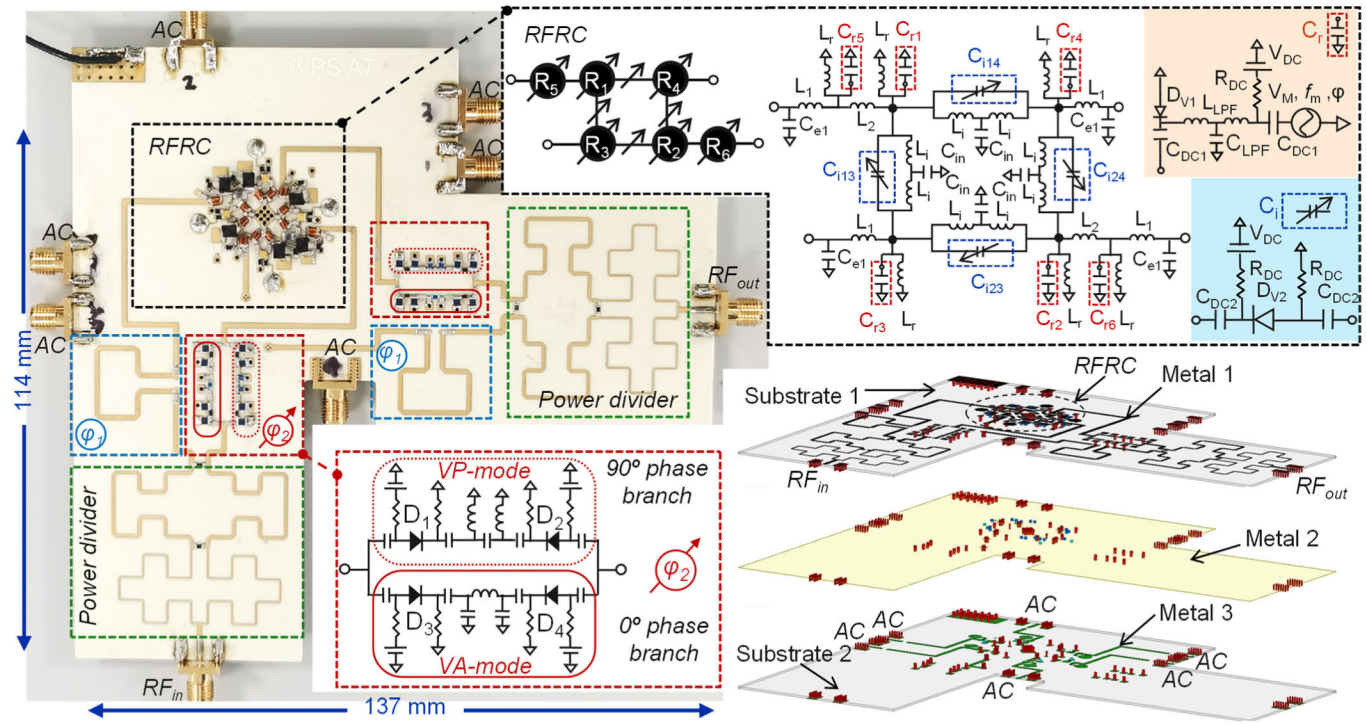

Fig. 12. Manufactured Prototype 1: multi-functinal component functionalising a single-band third order TF.

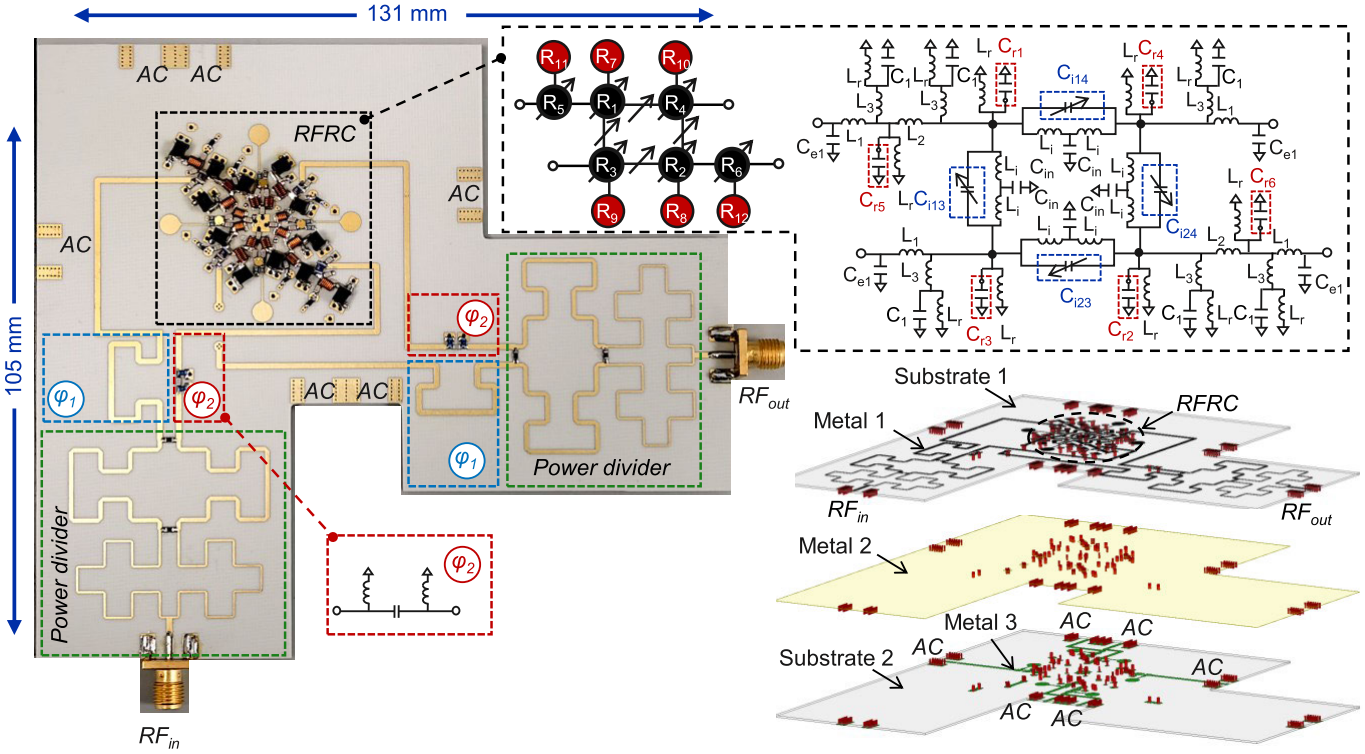

Fig. 13. Manufactured Prototype 2: multi-functinal component functionalising a dual-band third order TF.

row and third column, it can be observed that a larger f_m results in a wider 10 dB isolation BW (red curve) compared to a smaller f_m (blue curve), which provides higher D at the center frequency. Higher ξ enhances D but at the cost of increased IL. Large φ distorts the passbands and a φ of 65° provides the largest D. For the third order dual-band responses shown in Fig. 9(b), performance trade-offs can also be observed. Specifically, the increasing of f_m results in lower D for both bands and different values of f_m can be observed to obtain the highest D for the two bands (16 MHz for the

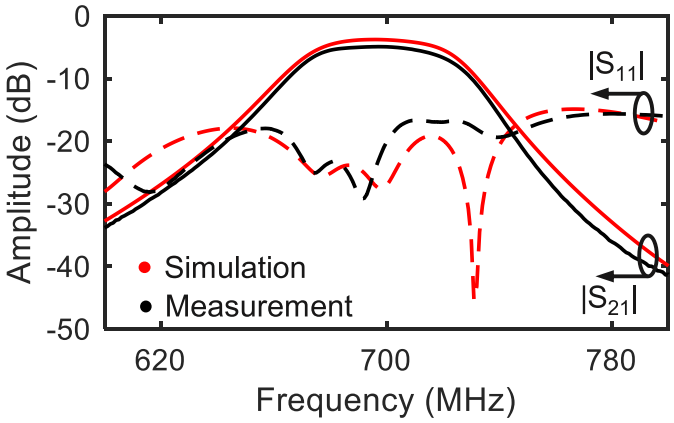

Fig. 14. Comparison between simulated and measured results for Prototype 1 at one tuning state.

lower band and 19 MHz for the upper band). Larger ξ leads to larger D for the lower band but smaller D at the upper band. While D increases for the upper band with an increase in φ, it first increases and then decreases for the lower band at the center frequency. Additionally, excessively large values of φ can distort the TF shapes for both bands. It can be noticed that the selection of STM parameters is application dependent. In this study, they are optimized to achieve high D within the passbands, while maintaining acceptable in-band IL.

C. Mode 2: RF Switching Mode

The proposed multi-functional RF component is also able to operate as an RF switch when φ_2-φ_1 =90°. Specifically, it can be intrinsically switched-off by setting the coupling element M_m to zero, while ensuring the couplings between R_1 and R_3, and R_2 and R_4, are identical as indicated in Fig. 10. In this configuration, the input RF signal reaches the output after being equally dived between two distinct signal paths (marked by green dotted and solid lines) that introduce a 180° phase difference and are subsequently cancelled. The intrinsically switched-off capabilities of the concept are demonstrated in Fig. 10 (green trace) for the same circuit configuration that was studied in the previous section.

D. Mode 3: RF Co-Designed Bandpass Filter, Isolator, Variable Attenuator (BPF/BPFI-VA)

The BPF-VA mode of operation can be obtained when $\varphi_2 = \varphi_1$, as shown in Fig. 1(c). Its operational behaviour can be described using equations (19)-(22). Specifically, as detailed in (20), the output power wave a_6 can be expressed in terms of the input power wave a_1, and can be adjusted from 0 to 1 by varying the power division ratio k from 0 to ∞. This is illustrated in Fig. 11 for the example case of the RFRC in Fig. 2 with three different tuning states. Specifically, when $k = 100$, 1 and 0.01 the attenuation is altered between 0, 3, 20 dB while the filtering TF and phase response remain unaltered. The same parametric studies can be performed at BPFI/VA mode to obtain the desirable modulation parameters

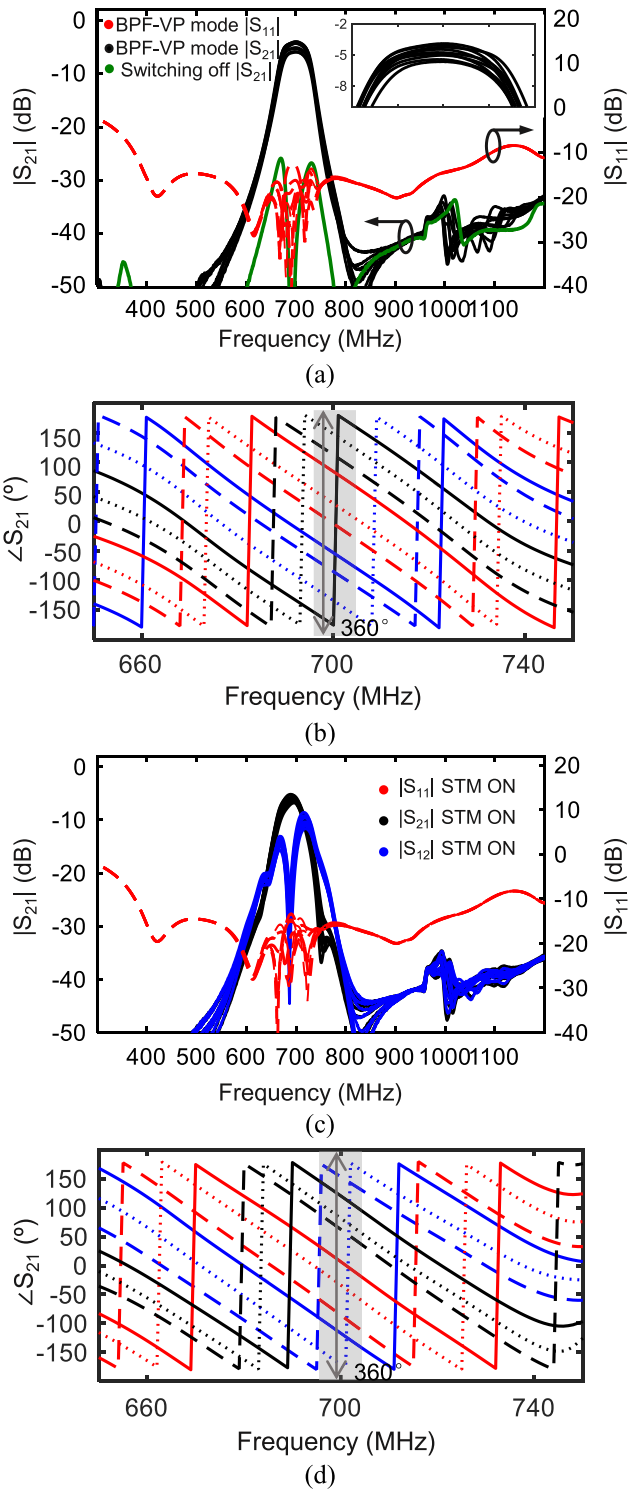

Fig. 15. RF-measured performance of the single-band prototype when configured in its BPF/BPFI-VP mode. (a), (b) Amplitude and phase responses when STM is OFF and is set in its BPF-VP mode of operation. (c), (d) Amplitude and phase responses when STM is ON and is set in its BPFI-VP mode of operation.

and they have been omitted for brevity.

$$a_2 = a_3 = \frac{a_1}{\sqrt{2}} e^{j\theta_{pd}} \tag{19}$$

$$a_4 = S_{c\_31} a_2 + S_{c\_32} a_3, a_5 = S_{c\_41} a_2 + S_{c\_42} a_3 \tag{20}$$

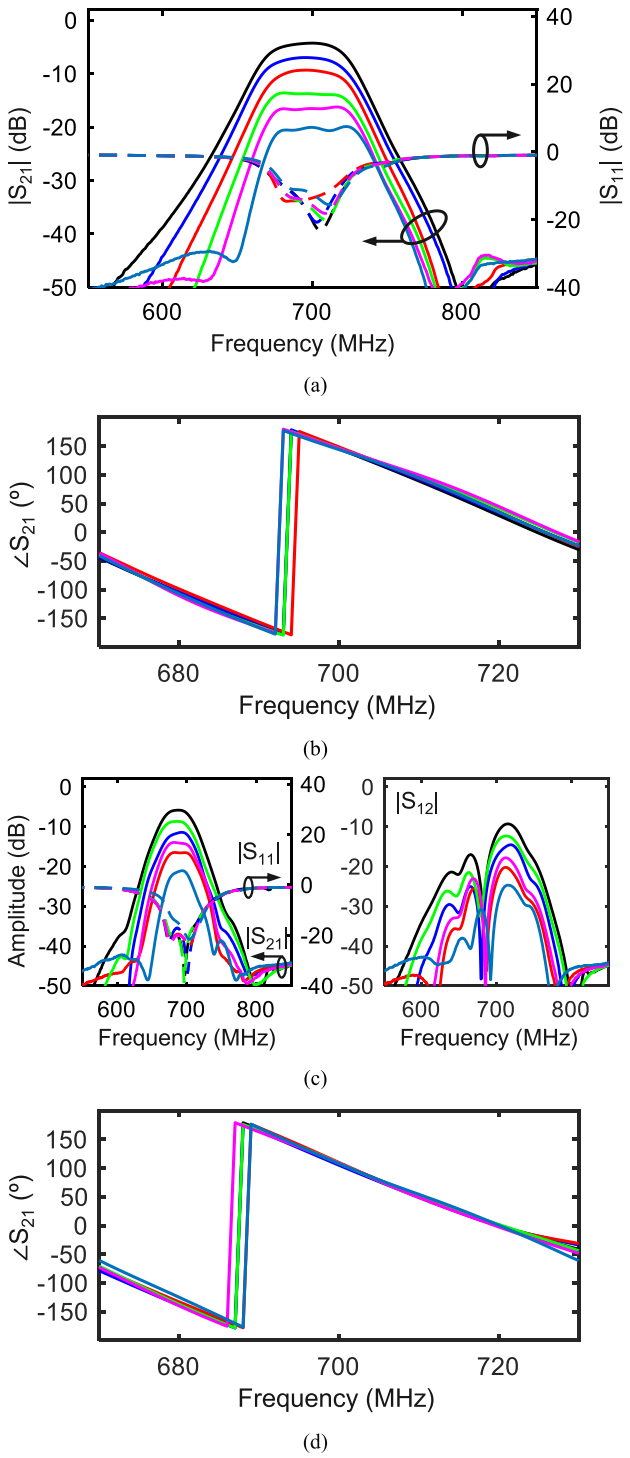

Fig. 16. RF-measured performance of the single-band prototype when configured in its BPF/BPFI-VA mode. (a), (b) Amplitude and phase responses when STM is OFF and is set in its BPF-VA mode of operation. (c), (d) Amplitude and phase responses when STM is ON and is set in its BPFI-VA mode of operation.

$$a_6 = \frac{\sqrt{2}}{2} e^{j\theta_{pd}} (a_5 + a_4) \tag{21}$$

$$|S_{21}| = \frac{|a_6|}{|a_1|} = \left| \frac{\sqrt{k}}{\sqrt{k+1}} \right| \tag{22}$$

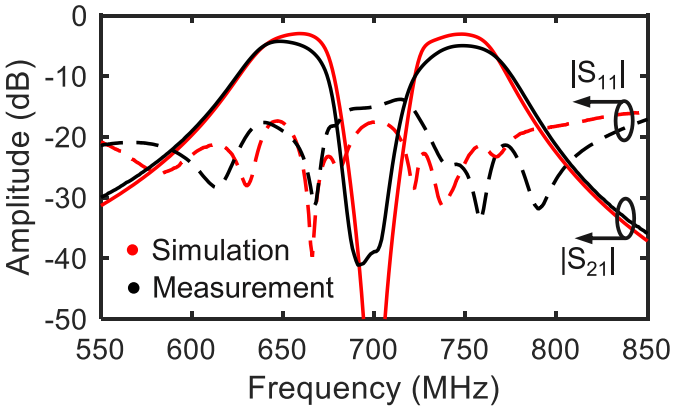

Fig. 17. Comparison between simulated and measured results for Prototype 2 at one tuning state.

III. Experimental Validation

To validate the multi-functional RF component concept, a single-band (Prototype 1) and a dual-band (Prototype 2) multi-functional prototypes were designed, manufactured, and characterized using as a reference the RFRCs in Fig. 8 and two wideband Wilkinson dividers. Specifically, static and reconfigurable phase coupling elements φ_1 and φ_2 were employed in Prototype 1 to facilitate the realization of three reconfigurable modes of operation: 1) single-band BPF/BPFI-VP, 2) intrinsic RF switching ON/OFF and 3) single-band BPF/BPFI-VA. Prototype 2 has been implemented with a constant phase difference φ_2-φ_1 equal to 90° allowing to realize two modes of operation, namely: 1) a dual-band BPF/BPFI-VP mode and 2) an RF switch mode. The two prototypes were implemented for a center frequency of 700 MHz and a fractional bandwidth of 10% and 15% using a dual-core multi-layer stack up comprising of two 0.508 mm-thick RO4003C substrates due to the need to realize a crossover as indicated in Fig. 1(a).

The manufactured prototypes are illustrated in Fig. 12 and 13 for the single-band and the dual-band prototype respectively. As it can be seen in Fig. 12, to facilitate the VP/VA reconfigurability in Prototype 1, a static phase coupling element φ_1 (in blue dashed boxes) and a switchable phase coupling element φ_2 (in red dashed boxes) are used to allow for a reconfigurable phase difference between 0° and 90° between the two output ports by controlling the four PIN diodes D_1 to D_4. Specifically, when D_1 and D_2 are ON while D_3 and D_4 are OFF, a phase difference of 90° is enabled between φ_2 *and* φ_1, and the device is operating at the VP mode. On the contrary, the VA mode is enabled when D_1 and D_2 are OFF while D_3 and D_4 are ON. Prototype 2 adopts two static phase coupling elements φ_1 and φ_2 to facilitate a constant 90° phase difference at the two output ports. The detailed circuits of the RFRCs for the two prototypes are provided in the black dashed boxes when using lumped elements. Static inverters are implemented through their first-order π-type equivalent networks. Additionally, the circuits for the STM resonators and tunable couplings are distinctly highlighted in red and blue dotted boxes, respectively, located on the upper right side of Fig. 12. The RF performance of the two prototypes were

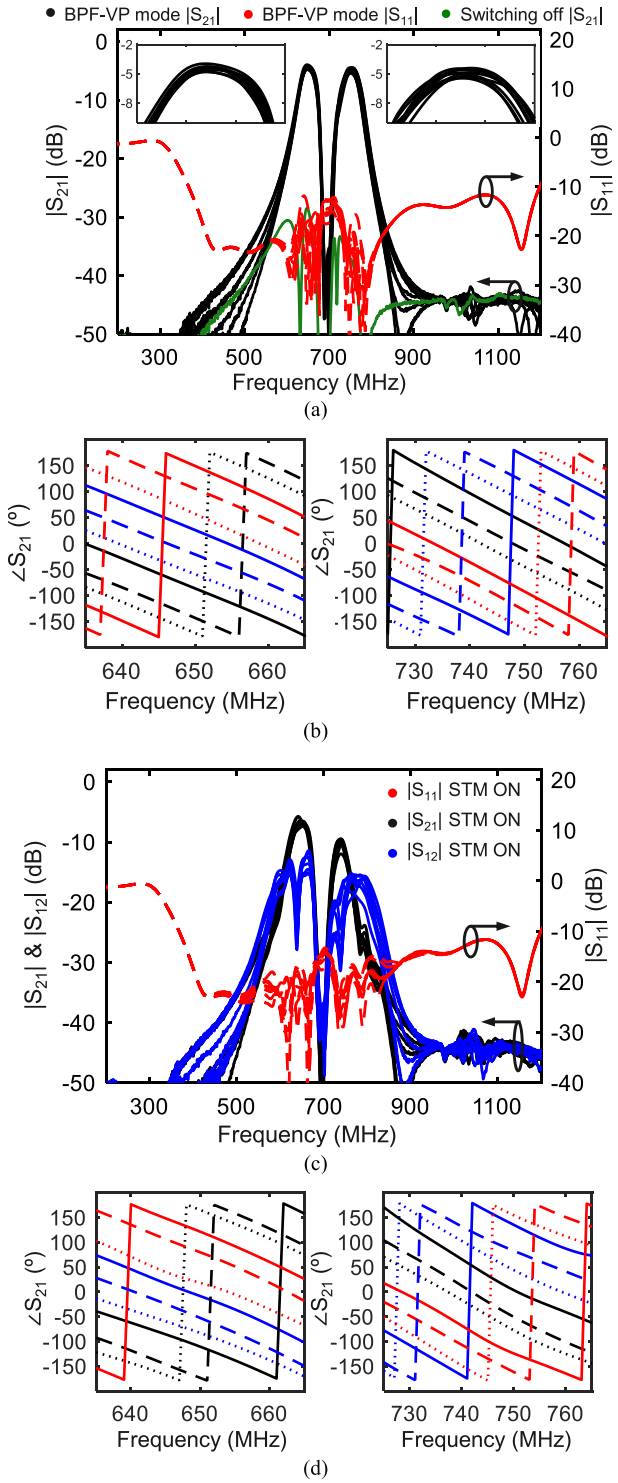

Fig. 18. RF-measured performance of the dual-band prototype when configured in its BPF/BPFI-VP mode. (a), (b) Amplitude and phase responses when STM is OFF and is set in its BPF-VP mode of operation. (c), (d) Amplitude and phase responses when STM is ON and is set in its BPFI-VP mode of operation.

characterized using a Keysight N5244A Network Analyzer. The required STM low-frequency RF signals were generated using arbitrary waveform generators.

The measured S-parameters for Prototype 1 are detailed in Figs. 14 to 16 for the three modes of operation. Specifically, Fig. 14 shows the comparison between simulated and measured results at one tuning state, demonstrating good agreement. Fig. 15 (a) depicts the performance of the multi-functional component when STM is OFF and operates in a BPF-VP mode of operation allowing for a full 360° phase tuning capability. Although nine distinct states are shown, its phase shift is continuously tunable. For these states, the IL was measured between 4 dB and 5.6 dB, alongside an input-reflectionless bandwidth (RBW) spanning from 375 MHz to 1093 MHz. The intrinsic switch-off mode of operation is also included in this figure (green trace). When STM is ON, the multi-functional component operates as a BPFI-VP, as depicted in Figs. 15(c), (d) for the exact same states as in Figs. 15(a), (b). As evidenced, its measured D is >20 dB at the center frequency for all tuning states while exhibiting a 360° phase variation range as observed in Fig. 15(d). The measured 20 dB isolation BW (the frequency range when $|S_{21}| > 20$ dB) vary from 11 MHz to 14 MHz. It can also be observed that when STM is ON, the insertion phase is offset for all states due to STM introducing both phase and amplitude non-reciprocity, a phenomenon has also been discussed in Fig. 3 of [54]. However, this phase shift remains constant when the modulation parameters are unchanged, ensuring that STM does not alter the overall phase tuning range of the device.

Fig. 16 details the performances of Prototype 1 in its BPF/BPFI-VA mode when φ_2- $\varphi_1 = 0°$. When STM is OFF and is configured in the BPF-VA mode of operation, a large attenuation tuning range can be obtained with its attenuation being continuously tunable between 4.2 dB to 20 dB as indicated in Fig. 16(a). The transmission zeros are generated by the mixed coupling within the filtering rat-race couplers. Adjusting these couplings to change the power division ratio also alters the frequency response of the equivalent network, thereby shifting the location of zeros. For all these states, the measured ripple levels are less than 0.1 dB for attenuation levels less than 13.7 dB. At higher attenuation levels, it can be observed that the ripple levels increase to 0.4 dB due to the dispersion of the lumped element-based coupler and manual tuning of varactors. As can be seen in Fig. 16(b), the insertion phase exhibits low phase imbalance to only 5° at the center frequency. Furthermore, when STM is ON, a $D > 20$ dB can be obtained for all tuning states as depicted in Fig. 16(c). The TF shape for all these tuning states remain well-preserved. For all these states, the IIP3 was measured between 14 dBm to 20 dBm.

The measurement results of Prototype 2 are concluded in Figs. 17 and 18. Fig. 17 shows the comparison between simulated and measured TFs at one tuning state, which are in good agreement. The degradation in the isolation slope, isolation level between the two bands, and band flatness is mainly due to the tolerances of the lumped components. In the topology shown in Fig. 8(b), the static resonators (in red) are used to create the notch between the two bands and must resonate at the same center frequency. However, tolerances in the corresponding capacitors and inductors result in slight variations in the resonating frequencies of these resonators. When STM is OFF, it works as BPF-VP with

TABLE I
COMPARISON WITH STATE-OF-ART CO-DESIGNED MULTI-FUNCTIONAL FILTERS

Ref.	Mode	f_{cen} (GHz)	TF	PTR (°)	ATR(dB) /PI(°)	RBW (GHz)	OFF	CTF	D (dB)	IL @ f_{cen} (dB)	Size ($(\lambda_g*\lambda_g)$)
T.W: P1	IS+VP	0.7	3rd BPF	360	No	0.72	Yes	Yes	>20	4~5.6 (STM OFF) 5.4~6.8 (STM ON)	0.6*0.5
	IS+VA	0.7	3rd BPF	No	15.8/<5	No			>20	4.2~20 (STM OFF) 5.8~21 (STM ON)	
T.W: P2	IS+VP	0.65; 0.745	3rd dual-band	360	No	0.83	Yes	Yes	>10	4.3~5.5 (STM OFF) 6.5~12 (STM ON)	0.58*0.46
[3]	VP	1.05~1.3	2nd BPF	320	No	No	No	No	No	4.1~5 @ 1.05 GHz	0.9*1.1
[4]	VP	0.6~0.71	4th BPF	175	No	No	No	Yes	No	1.9~3	0.67*0.37
[5]	VP	0.65~0.86	3rd BPF	360	No	No	No	No	No	2.4~4.3 @ 0.65 GHz	0.14*0.14
[6]	VP	1.07~1.36	3rd BPF	90	No	No	No	Yes	No	0.8~1.4	0.31*0.27
[29]	VP	0.69	2nd BPF	340	No	No	No	Yes	10	5.9~6.9	0.3*0.3
[14]	VA	1	3rd BPF	No	8/<1.5	No	No	Yes	No	2~10	0.145*0.29
[16]	VA	1.01~1.19	2nd BPF	No	18/N/A	No	No	No	No	3.3~21.5	1.02*0.72
[18]	VA	2	5th BPF	No	14/N/A	No	No	Yes	No	2.76~16.99	0.36*0.31
[19]	VA+VP	0.75~0.95	2nd BPF	360	10/0~8	No	No	No	No	5.3~6.6(VP) 5.3~15(VA)	0.48*0.4
[25]	IS	0.88~1.03	3rd BPF	No	No	No	No	N/A	>20	3.9 (STM OFF) 5.2 (STM ON)	0.26*0.1
[28]	IS	0.6~0.68; 0.72~0.83	3rd dual-band	No	No	No	No	N/A	>20	4.8~6.2 (STM ON)	0.28*0.24

T.W: This work, P1: Prototype 1, P2: Prototype 2, TF: transfer function, PTR: phase tuning range, ATR: attenuation tuning range, PI: phase imbalance at center frequency, RBW: reflectionless bandwidth, OFF: intrinsic switching off capability, CTF: constant transfer function, D: directivity at center frequency, IL: insertion loss, IS: isolator, VA: variable attenuator, VP: variable phase shifter.

the measured amplitude responses provided in Fig. 18(a) and phase responses in Fig. 18(b). It can be observed from Fig. 18(a) that third order dual-band transfer functions are generated and the continuously phase tuning is achieved for both bands as indicated in Fig. 18(b), resulting a 360° phase tuning range in total. IL for both bands varies from 4.3 dB to 5.5 dB with a large RBW ranging from 368 MHz to 1200 MHz. The measured performance of its switching off mode is also included in Fig. 18(a) shown as the green trace with an isolation level of $>$ 30 dB. When STM is ON, the multi-functional device works at its BPFI-VP mode with uni-directional transmission for both bands. Fig. 18(c) showcases enabled uni-directional transmission for both bands. In this case, the 18 dB isolation BW for the lower band varies from 6 MHz to 14 MHz. For the upper band, D is more than 10 dB for all the tuning cases at the center frequency of 733 MHz. A degradation of the IL and isolation can be observed for the upper band due to its higher sensitivity to variations in the capacitance and inductance values of the notch resonators. It is noted that across all displayed states for both BPF/BPFI-VP modes, the TFs for both bands are well preserved. The measured IIP3 across all these tuning states ranges from 17 dBm to 24 dBm.

A comparison of the proposed multi-functional BPF concept with SOA co-designed BPFs, VPs/VAs and ISs is provided in Table I. As evidenced, Prototype 1 achieves the largest phase tuning range with well-preserved transfer functions as opposed to the VPs in [3], [4], [5], [6], and [29] that have lower phase tuning range and distorted TF. Furthermore, through the manufacturing and testing of Prototype 2, this paper demonstrates for the first time the potential to functionalize a dual-band TF exhibiting three multi-functional modes of operation as a unique advantage to be highlighted in relation to the SOA. In addition, this concept facilitates the realization of a reflectionless filtering TF, an additional RF switching-off mode of operation and also incorporates the functionality of an isolator with D $>$ 20 dB. These operational features haven't been demonstrated in any of the existing VP topologies in Table I. When comparing the performance of the proposed multi-functional circuit with the VAs in [14] and [18], Prototype 1 exhibits a larger attenuation tuning range. While the VAs in [16] offer a wider attenuation tuning, they experience considerable variations in the TF shape and return loss during the tuning process. Additionally, the proposed BPFI-VA is also the only one to integrate an isolator function to a VA, achieving a D of more than 20 dB in all tuning states. Although [19] allows for both phase and attenuation adjustments, its attenuation range is limited, and tuning its phase or attenuation significantly alters the TFs. When comparing with the BPFIs that enable uni-directional transmission for single band [25] or multi-band [28] TFs, the proposed multi-functional device supports more functionalities and can work as a VP or VA. The relatively high IL in the proposed multi-functional component is due to the use of lossy LEs having moderate quality factors (e.g, 80-200 for inductors and 50-75 for varactors) as also observed in LE-based RF component implementations. However, given the multi-functional nature of this circuit, integrating four functionalities, the IL is reasonable and comparable to other co-designed RF filters, such as those in [19], with IL ranging

from 5.2 to 6.6 dB. When compared to state-of-the-art multi-functional filters, the dimensions of the proposed component are similar to those in [3], [4], and [16]. Although some other devices have slightly smaller sizes, the proposed device offers additional functionalities.

Although the proposed concept builds upon the work in [47], it is significantly expanded and offers unique contributions. These include: 1) the addition of an in-depth theoretical analysis of the filtering rat-race coupler. Specifically, it provides a comprehensive even and odd mode analysis, detailing the scattering matrix equations in terms of the coupling matrix values, which is crucial for maintaining a consistent transfer function and return loss, especially in variable phase shifter and attenuator modes, 2) a unique equivalent circuit method (Figs. 2 to 6) that simplifies the analysis and implementation of various filter topologies, 3) demonstrating scalability of the method to higher-order and quasi-elliptic as well as multi-band transfer functions through different CRD topologies, 4) extending its functionality to multi-band and non-reciprocal transfer function realizations, validated through new prototypes, showcasing advancements not presented in [47]. Overall, the proposed multi-functional device is the only co-designed BPF that combines multiple tunable modes of operation with high levels of flexibility, multi-band capabilities, intrinsic switching off operation, reflectionless transfer function, and unidirectional transmission.

IV. Conclusion

This paper reports on an innovative RF co-design method for designing multi-function devices capable of serving as BPFs with single-/dual-band TFs, VPs, VAs, RF switches and ISs. The methodology is validated at 700 MHz through two prototypes, showcasing the ability to obtain both single- and dual-band bandpass TFs. Prototype 1 demonstrates three distinct modes of operation: 1) BPF/BPFI-VP mode, 2) RF switch mode, and 3) BPF/BPFI-VA mode. In the BPF-VP mode, it features a third order bandpass TF with a 360° phase tuning range and a broad RBW spanning 375 to 1093 MHz. The BPF-VA mode offers a third-order bandpass TF with an attenuation range from 4.2 dB to 20 dB as well as a low phase imbalance of $<5°$. Both BPFI-VP mode and BPFI-VA mode exhibit unidirectional transmission with a D exceeding 20 dB. Prototype 2 is designed to facilitate a third-order dual-band bandpass TF with BPF/BPFI-VP mode and RF switching off mode. A continuously tunable phase shift of 360° with a RBW spanning from 368 MHz to 1200 MHz is demonstrated for both bands at BPF/BPFI-VP working mode as well as a D >10 dB at BPFI-VP mode. It should be noted that the filtering TFs across all operational states for both prototypes are well preserved.

References

[1] D. Morikawa, H. Deguchi, M. Tsuji, and H. Shigesawa, "A microstrip-line phase shifter constructed by a tunable filter," *Electron. Commun. Jpn.*, vol. 90, no. 2, pp. 25–32, Feb. 2007.

[2] R. Lovato and X. Gong, "A low-loss continuously tunable phase shifter based on a bandpass filter with reconfigurable transmission zeros," in *IEEE MTT-S Int. Microwave Symp. Dig.*, Boston, MA, USA, Jun. 2019, pp. 849–852.

[3] X. Zhu, T. Yang, P.-L. Chi, and R. Xu, "Novel passive vector-sum reconfigurable filtering phase shifter with continuous phase-control and tunable center frequency," *IEEE Trans. Microwave Theory Techn.*, vol. 70, no. 2, pp. 1188–1197, Feb. 2022.

[4] X. Chen, C. Yi, P.-L. Chi, and T. Yang, "Novel synthesis method for reconfigurable filtering phase shifter with frequency-dependent coupling using optimization technique," *IEEE Trans. Circuits Syst. II, Exp. Briefs*, vol. 70, no. 4, pp. 1400–1404, Apr. 2023.

[5] X. Chen, Z. Wei, P.-L. Chi, and T. Yang, "Design and synthesis of reconfigurable filtering phase shifter using optimization of coupling matrix," *IEEE Trans. Microwave Theory Techn.*, vol. 70, no. 8, pp. 3886–3896, Aug. 2022.

[6] H. Li, X. Guo, L. Zhu, and W. Wu, "Design of wideband tunable filtering phase shifter with switchable TTD or CPD phase mode," *IEEE Trans. Circuits Syst. II, Exp. Briefs*, vol. 71, no. 1, pp. 101–105, Jan. 2024.

[7] J. Bae and C. Nguyen, "A 44 GHz CMOS RFIC dual-function attenuator with band-pass-filter response," *IEEE Microwave Wireless Compon. Lett.*, vol. 25, no. 4, pp. 241–243, Apr. 2015.

[8] A. Moradinia, C. D. Cheon, C. T. Coen, N. E. Lourenco, A. S. Cardoso, and J. D. Cressler, "A 42.5–51.0 GHz SiGe BiCMOS integrated tunable bandpass filter and attenuator," in *Proc. IEEE BiCMOS Compound Semicond. Integr. Circuits Technol. Symp. (BCICTS)*, Oct. 2022, pp. 183–186.

[9] B. Wu et al., "Dynamically tunable filtering attenuator based on graphene integrated microstrip resonators," *IEEE Trans. Microwave Theory Techn.*, vol. 68, no. 12, pp. 5270–5278, Dec. 2020.

[10] R. Hou, J. Chen, Y.-T. Zhao, T. Su, L. Li, and K.-D. Xu, "Varactor-graphene-based bandpass filter with independently tunable characteristics of frequency and amplitude," *IEEE Trans. Compon., Packag., Manuf. Technol.*, vol. 12, no. 8, pp. 1375–1385, Aug. 2022.

[11] Z.-C. Lin et al., "Dual-band bandpass filter with independently tunable attenuation characteristics using graphene nanoplates," *IEEE Trans. Plasma Sci.*, vol. 50, no. 12, pp. 5031–5037, Dec. 2022.

[12] J. M. Knowles, H. H. Sigmarsson, and J. W. McDaniel, "Design of a symmetric lumped-element bandpass filtering attenuator (Filtenuator)," in *Proc. IEEE 22nd Annu. Wireless Microwave Technol. Conf. (WAMICON)*, Apr. 2022, pp. 1–4.

[13] J. M. Knowles, H. H. Sigmarsson, and J. W. McDaniel, "Higher-order filtering attenuator design considerations for filter shape optimization," in *Proc. IEEE Wireless Microwave Technol. Conf. (WAMICON)*, Melbourne, FL, USA, Apr. 2023, pp. 85–88.

[14] J. M. Knowles, H. H. Sigmarsson, and J. W. McDaniel, "Generalized theory and realization of continuously loss-programmable bandpass filtering attenuators," *IEEE Trans. Microwave Theory Techn.*, vol. 71, no. 12, pp. 1–15, Dec. 2023.

[15] J. Li, W. He, K.-D. Xu, J. Chen, and X. Y. Zhang, "Compact tunable broadband filtering attenuator based on variable resistors," *IEEE Microwave Wireless Technol. Lett.*, vol. 33, no. 7, pp. 983–986, Jul. 2023.

[16] Z. Wei, S. Chen, X. Zhu, P.-L. Chi, R. Xu, and T. Yang, "Reconfigurable filtering attenuator with continuously tunable center frequency and amplitude," in *IEEE MTT-S Int. Microwave Symp. Dig.*, Denver, CO, USA, Jun. 2022, pp. 187–190.

[17] B. Pal, M. K. Mandal, M. Kahar, and S. Dwari, "Filtering attenuator with electronically tunable attenuation," in *Proc. IEEE MTT-S Int. Microwave RF Conf.*, vol. 90, no. 2, 2021, pp. 1–4.

[18] W. He, J. Li, K.-D. Xu, S. Yan, and J. Chen, "Voltage-controlled tunable filtering attenuator using PIN diodes," *IEEE Trans. Circuits Syst. II, Exp. Briefs*, vol. 71, no. 2, pp. 562–566, Feb. 2024.

[19] Z. Wei, X. Chen, X. Zhu, P. Chi, R. Xu, and T. Yang, "Novel passive vector-sum amplitude-variable phase shifter with integrated reconfigurable filtering function," *IEEE Trans. Microwave Theory Techn.*, vol. 70, no. 7, pp. 3511–3523, Jul. 2022.

[20] D. Regev et al., "Analysis and design of quasi-circulating quadrature hybrid for full-duplex wireless," *IEEE Trans. Circuits Syst. I, Reg. Papers*, vol. 68, no. 12, pp. 5168–5181, Dec. 2021.

[21] H. Dong, J. R. Smith, and J. L. Young, "A wide-band, high isolation UHF lumped-element ferrite circulator," *IEEE Microwave Wireless Compon. Lett.*, vol. 23, no. 6, pp. 294–296, Jun. 2013.

[22] A. Ashley and D. Psychogiou, "RF co-designed bandpass filter/circulator with tunable center frequency, bandwidth, and out-of-band isolation," *IEEE Microwave Wireless Compon. Lett.*, vol. 31, no. 7, pp. 845–848, Jul. 2021.

[23] J. Chang, J. Kao, Y. Lin, and H. Wang, "Design and analysis of 24-GHz active isolator and quasi-circulator," *IEEE Trans. Microwave Theory Techn.*, vol. 63, no. 8, pp. 2638–2649, Aug. 2015.

[24] S. A. Ayati, D. Mandal, B. Bakkaloglu, and S. Kiaei, "Integrated quasi-circulator with RF leakage cancellation for full-duplex wireless transceivers," *IEEE Trans. Microwave Theory Techn.*, vol. 66, no. 3, pp. 1421–1430, Mar. 2018.

[25] X. Wu, M. Nafe, A. Á. Melcón, J. S. Gómez-Díaz, and X. Liu, "Frequency tunable non-reciprocal bandpass filter using time-modulated microstrip $\lambda_g/2$ resonators," *IEEE Trans. Circuits Syst. II, Exp. Briefs*, vol. 68, no. 2, pp. 667–671, Feb. 2021.

[26] G. Chaudhary and Y. Jeong, "Nonreciprocal bandpass filter using mixed static and time-modulated resonators," *IEEE Microwave Wireless Compon. Lett.*, vol. 32, no. 4, pp. 297–300, Apr. 2022.

[27] P. Dutta, G. A. Kumar, and G. Ram, "Numerical design of non-reciprocal bandpass filters with the aid of 3D coupling matrix for 5G bands," *IEEE Trans. Circuits Syst. II, Exp. Briefs*, vol. 69, no. 7, pp. 3334–3338, Jul. 2022.

[28] Z. Zhang and D. Psychogiou, "Incorporating directionality in transversal-resonator-based bandpass filters with tunable transfer function characteristics," *IEEE Trans. Circuits Syst. I, Reg. Papers*, vol. 70, no. 12, pp. 5194–5207, Dec. 2023.

[29] Z. Zhang and D. Psychogiou, "Non-reciprocal RF co-designed filtering phase shifters with continuously tunable phase shift," in *Proc. 53rd Eur. Microwave Conf. (EuMC)*, Berlin, Germany, Sep. 2023, pp. 102–105.

[30] V. Szortyka, K. Raczkowski, M. Kuijk, and P. Wambacq, "A wideband beamforming lowpass filter for 60 GHz phased-array receivers," *IEEE Trans. Circuits Syst. I, Reg. Papers*, vol. 62, no. 9, pp. 2324–2333, Sep. 2015.

[31] H. Zhu, H. Sun, B. Jones, C. Ding, and Y. J. Guo, "Wideband dual-polarized multiple beam-forming antenna arrays," *IEEE Trans. Antennas Propag.*, vol. 67, no. 3, pp. 1590–1604, Mar. 2019.

[32] S. V. Hum and J. Perruisseau-Carrier, "Reconfigurable reflectarrays and array lenses for dynamic antenna beam control: A review," *IEEE Trans. Antennas Propag.*, vol. 62, no. 1, pp. 183–198, Jan. 2014.

[33] Y.-H. Nam et al., "Full-dimension MIMO (FD-MIMO) for next generation cellular technology," *IEEE Commun. Mag.*, vol. 51, no. 6, pp. 172–179, Jun. 2013.

[34] D. Zhao et al., "Millimeter-wave integrated phased arrays," *IEEE Trans. Circuits Syst. I, Reg. Papers*, vol. 68, no. 10, pp. 3977–3990, Oct. 2021.

[35] I. Kalyoncu, A. Burak, and Y. Gurbuz, "A K-band 5G phased array RX channel with 3.3-dB NF and 28.5-dB gain in 130-nm SiGe," *IEEE Trans. Circuits Syst. II, Exp. Briefs*, vol. 67, no. 12, pp. 2938–2942, Dec. 2020.

[36] Y. Zheng and C. E. Saavedra, "Full 360° vector-sum phase-shifter for microwave system applications," *IEEE Trans. Circuits Syst. I, Reg. Papers*, vol. 57, no. 4, pp. 752–758, Apr. 2010.

[37] T.-W. Li and H. Wang, "A millimeter-wave fully integrated passive reflection-type phase shifter with transformer-based multi-resonance loads for 360° phase shifting," *IEEE Trans. Circuits Syst. I, Reg. Papers*, vol. 65, no. 4, pp. 1406–1419, Apr. 2018.

[38] W. J. Liu, S. Y. Zheng, Y. M. Pan, Y. X. Li, and Y. L. Long, "A wideband tunable reflection-type phase shifter with wide relative phase shift," *IEEE Trans. Circuits Syst. II, Exp. Briefs*, vol. 64, no. 12, pp. 1442–1446, Dec. 2017.

[39] B. W. Xu, S. Y. Zheng, W. M. Wang, Y. L. Wu, and Y. A. Liu, "A coupled line-based coupler with simultaneously tunable phase and frequency," *IEEE Trans. Circuits Syst. I, Reg. Papers*, vol. 66, no. 12, pp. 4637–4647, Dec. 2019.

[40] P. Gu, D. Zhao, and X. You, "Analysis and design of a CMOS bidirectional passive vector-modulated phase shifter," *IEEE Trans. Circuits Syst. I, Reg. Papers*, vol. 68, no. 4, pp. 1398–1408, Apr. 2021.

[41] A. Singh and M. K. Mandal, "Electronically tunable reflection type phase shifters," *IEEE Trans. Circuits Syst. II, Exp. Briefs*, vol. 67, no. 3, pp. 425–429, Mar. 2020.

[42] C. Shao, H. Chu, X. Zhu, and Y. Guo, "Tunable phase shifter with small phase error and insertion loss fluctuation using a resonator-based structure," *IEEE Trans. Circuits Syst. II, Exp. Briefs*, vol. 70, no. 1, pp. 11–15, Jan. 2023.

[43] F. Wei, X.-Z. Ding, X. Liu, B. Liu, Z. Li, and X.-B. Zhao, "Balanced filtering phase shifters with low phase deviation and high common-mode suppression," *IEEE Trans. Circuits Syst. I, Reg. Papers*, vol. 70, no. 7, pp. 2814–2822, Jul. 2023.

[44] Q. Dong, Y. Wu, W. Chen, Y. Yang, and W. Wang, "Single-layer dual-band bandwidth-enhanced filtering phase shifter with two different predetermined phase-shifting values," *IEEE Trans. Circuits Syst. II, Exp. Briefs*, vol. 68, no. 1, pp. 236–240, Jan. 2021.

[45] L.-L. Qiu and L. Zhu, "Synthesis design of filtering differential phase shifters of independently suppressed harmonics," *IEEE Trans. Circuits Syst. II, Exp. Briefs*, vol. 68, no. 8, pp. 2760–2764, Aug. 2021.

[46] L. Feng, J. Chen, X. Yu, L. Zhu, and H. Liu, "A novel wideband 90° filtering phase shifter using broadside-coupled MSLs," *IEEE Trans. Circuits Syst. II, Exp. Briefs*, vol. 69, no. 6, pp. 2742–2746, Jun. 2022.

[47] Z. Zhang and D. Psychogiou, "Multifunctional bandpass filter with code-signed tunable attenuator and reflectionless phase shifter functionalities," *IEEE Microwave Wireless Technol. Lett.*, vol. 34, no. 6, pp. 737–740, Jun. 2024, doi: 10.1109/LMWT.2024.3377266.

[48] U. Rosenberg, M. Salehi, S. Amari, and J. Bornemann, "Compact multi-port power combination/distribution with inherent bandpass filter characteristics," *IEEE Trans. Microwave Theory Techn.*, vol. 62, no. 11, pp. 2659–2672, Nov. 2014.

[49] J. Bornemann, U. Rosenberg, S. Amari, and S. S. Hesari, "Design of sum-difference power combiners with second-order filtering functions," in *IEEE MTT-S Int. Microwave Symp. Dig.*, May 2017, pp. 296–298.

[50] J.-S. Hong and M. J. Lancaster, *Microstrip Filters for RF/Microwave Applications*. Hoboken, NJ, USA: Wiley, 2004.

[51] D. Simpson and D. Psychogiou, "Fully-reconfigurable non-reciprocal bandpass filters," in *IEEE MTT-S Int. Microwave Symp. Dig.*, Aug. 2020, pp. 807–810.

[52] G. Macchiarella and S. Tamiazzo, "Design techniques for dualpass-band filters," *IEEE Trans. Microwave Theory Techn.*, vol. 53, no. 11, pp. 3265–3271, Nov. 2005.

[53] R. Gómez-García and A. C. Guyette, "Reconfigurable multi-band microwave filters," *IEEE Trans. Microwave Theory Techn.*, vol. 63, no. 4, pp. 1294–1307, Apr. 2015.

[54] X. Wu, X. Liu, M. D. Hickle, D. Peroulis, J. S. Gómez-Díaz, and A. Á. Melcón, "Isolating bandpass filters using time-modulated resonators," *IEEE Trans. Microwave Theory Techn.*, vol. 67, no. 6, pp. 2331–2345, Jun. 2019.

Zixiao Zhang (Graduate Student Member, IEEE) received the bachelor's and master's degrees from the Huazhong University of Science and Technology in 2016 and 2019, respectively. She is currently pursuing the Ph.D. degree in electrical and electronic engineering with University College Cork (UCC), Ireland. Her current research interests include synthesis, design, and characterization of reconfigurable RF components.

Dimitra Psychogiou (Senior Member, IEEE) received the Dipl.-Eng. degree in electrical and computer engineering from the University of Patras, Patras, Greece, in 2008, and the Ph.D. degree in electrical engineering from the Swiss Federal Institute of Technology (ETH), Zürich, Switzerland, in 2013. She was a Sr. Research Scientist with Purdue University, West Lafayette, IN, USA, and an Assistant Professor with the University of Colorado Boulder (UC Boulder), Boulder, CO, USA. She is currently a Professor of electrical and electronic engineering with University College Cork (UCC) and the Head of the Advanced RF Technology Group, Tyndall National Institute, Cork, Ireland. Her research has been presented in more than 230 publications. Her current research interests include RF design and characterization of reconfigurable microwave and millimeter-wave passive components, RF-MEMS, acoustic wave resonator-based filters, tunable filter synthesis, frequency-agile antennas, and additive manufacturing technologies for 3-D antenna sub-systems. She is a Senior Member of URSI and a member of the IEEE MTT-S Filters and Passive Components (MTT-5) and Microwave Control Materials and Devices (MTT-13) Committees. She has received multiple awards, including the 2023 IEEE MTT-S Outstanding Young Engineer Award, the 2021 Roberto Sorrentino Prize, the SFI Research Professorship Award, the 2020 NSF CAREER Award, the 2020 URSI Young Scientist Award, and the Junior Faculty Outstanding Research Award from UC Boulder. Furthermore, she serves on the Technical Review Board of various IEEE and EuMA conferences and journals. She is the Chair of MMT-13 and the Secretary of USNC-URSI Commission D. She was an Associate Editor of the *IET Microwaves, Antennas and Propagation* journal. She is an Associate Editor of the IEEE MICROWAVE AND WIRELESS COMPONENTS LETTERS and the *International Journal of Microwave and Wireless Technologies*.